# Flow and heat transfer mechanism of wall mode in Rayleigh-Bénard convection under strong magnetic fields

Kai Wu, Long Chen,* and Ming-Jiu Ni
*School of Engineering Science, University of Chinese Academy of Sciences, Beijing 101408, China*

(Received 10 December 2024; accepted 6 March 2025; published 28 March 2025; corrected 3 February 2026)

Direct numerical simulations have been performed to investigate the quasistatic magnetoconvection of a low Prandtl number fluid (Pr = 0.025) within a rectangular cell of varying aspect ratios under the influence of a vertical magnetic field. The Hartmann number (Ha) is fixed at Ha = 200 and Ha = 1000, while the Rayleigh number (Ra) ranges from $2 \times 10^5$ to $1 \times 10^7$, encompassing the entire region of the wall mode. Under a strong magnetic field, sidewall instability triggers convection onset, leading to wall mode states with enhanced heat transfer. As Ra increases, wall mode expands towards the cell center, increasing heat transfer intensity, as indicated by the Nusselt number (Nu). Reducing the aspect ratio and increasing the magnetic field both improve global Nu by enlarging the wall-mode region and intensifying heat transfer within it. This study introduces a root-mean-square velocity-based method for characterizing the wall mode, revealing significant circulation in the bulk. It also analyzes the double-layer structure of the wall mode, where the core and reverse flows are driven by buoyancy with an anomalous weakening of the Lorentz force in the core. A thermal boundary layer is observed in the impact zone, correlating inversely with heat transfer intensity.

DOI: 10.1103/PhysRevFluids.10.033702

## I. INTRODUCTION

In natural phenomena such as stellar and planetary systems, as well as in industrial contexts such as alloy solidification and nuclear fusion reactors, thermal convection in electrically conducting fluids subjected to magnetic fields is pervasive [1,2]. Despite the shared physical principles underlying these systems, our comprehension of electromagnetic thermal convection remains constrained, primarily due to the inherent complexities of experimental and computational approaches [3]. Experimental studies of liquid metal flows under strong magnetic fields are particularly hindered by the opacity of such metals, which precludes the use of conventional optical measurement techniques. Numerically, the challenges are equally formidable, as the development of accurate computational schemes and the substantial computational resources demanded by these conditions impose significant barriers. As a result, our understanding of wall-bounded liquid metal flows, their behavior under intense magnetic fields, and the unifying characteristics across varying field strengths and geometric aspect ratios remains superficial, with profound insights still elusive.

Through linear stability analysis, the critical Ra for the onset of thermal convection in an infinite periodic horizontal layer subjected to a vertical magnetic field can be determined [4,5]. This critical value, denoted as $\mathrm{Ra}_c$, signifies the initiation of convection in the bulk of the system. The analysis reveals that buoyancy-driven convection must counterbalance both viscous forces and Joule dissipation, implying that magnetic fields inherently suppress the onset of convection.

*Contact author: chenlong@ucas.ac.cn

 

The conditions for the emergence of steady magnetoconvection in an infinite plane layer can be expressed as derived by Chandrasekhar [5]:

$$\mathrm{Ra}_c = \frac{\pi^2 + a^2}{a^2}[(\pi^2 + a^2)^2 + \pi^2 \mathrm{Ch}]. \tag{1}$$

Here, $a$ represents the aspect ratio of the characteristic cell, defined as $a = \pi H/L$, where $H$ is the height of the fluid layer, $2L$ is the horizontal wavelength of convection, and $\mathrm{Ch} = \mathrm{Ha}^2 = B_0^2 H^2 \sigma/(\rho\nu)$ is the dimensionless magnetic field strength, where $B_0$ is the external magnetic field strength, $\sigma$ is the electrical conductivity, $\rho$ is the mass density, $\nu$ is the kinematic viscosity. Assuming the flow exists in the form of two-dimensional rolls, each roll has a diameter of $L$. By minimizing the aforementioned equation and setting $\partial \mathrm{Ra}/\partial a = 0$, we can obtain the critical $\mathrm{Ra}_c^\infty \longrightarrow \pi^2 \mathrm{Ch}$ for steady magnetoconvection in an infinite layer with free-slip boundaries at both ends.

Studies conducted on a semi-infinite slab with side walls [6] elucidate the onset of thermal convection influenced by the presence of side walls. An asymptotic solution valid at large Ch for the semi-infinite domain, bounded by free-slip upper and lower surfaces along a vertical side wall, can be formulated [6]. The critical Rayleigh number, $\mathrm{Ra}_w$, for these so-called magnetic wall modes is given by:

$$\mathrm{Ra}_w = 3\pi^2\sqrt{3\pi/2}(1 + 3\mathrm{Ch}^{-1/4}\sqrt{3\pi/2})\mathrm{Ch}^{3/4}. \tag{2}$$

The two values of the Rayleigh number (Ra) obtained from theoretical analysis have been thoroughly corroborated by both numerical simulations and experimental observations, as reported in the studies by Liu *et al.* [7] and Xu *et al.* [8]. In the presence of a strong magnetic field, the relationship $\mathrm{Ch}^{\frac{3}{4}} \ll \mathrm{Ch}$ holds true. As a consequence, the onset value of the Rayleigh number for the wall mode, denoted as $\mathrm{Ra}_w$, is lower than the onset value of the Rayleigh number for bulk convection, $\mathrm{Ra}_c$. This difference in critical values implies that there is a distinct wall-mode flow state existing between these two critical Ra values. It is important to note that Busse's formula 4 for calculating $\mathrm{Ra}_w$ is applicable only within the asymptotic limit of large values of the Chandrasekhar number (Ch). Moreover, the original formulation of Busse's formula assumes free-slip boundaries, rather than no-slip boundaries. For the case of no-slip boundaries, relevant estimates have been provided in the work of Xu *et al.* [8].

Figure 1 provides a comprehensive overview of the parameter space explored, where the red lines denote the critical $\mathrm{Ra}_w$ for the onset of convection in a semi-infinite convection layer, while the black lines indicate the critical $\mathrm{Ra}_c$ for convection onset in an infinite convection layer. This paper carefully selects parameters from preexisting studies, encompassing both experimental and simulation-based research. Specifically, in the work of Xu *et al.* [8], direct numerical simulations (DNS) were conducted on several typical parameters used in experiments. This paper selects the DNS parameters from their study. Notably, existing papers did not have an exclusive focus on the wall mode. As a result, the parameter span in their study is relatively wide. In sharp contrast, the parameters chosen in the present study are all carefully confined within the range relevant to the wall mode. This targeted selection of parameters allows for a more in-depth and focused exploration of the wall-mode phenomena, enabling a more accurate analysis and understanding of the specific physical processes and characteristics associated with the wall mode.

We systematically examine the effects of liquid metal convection in a closed square cell with aspect ratios $\Gamma = d/H = 2, 4$, where $d$ is the width of the cell, by keeping $d = 1$ and adjusting the height $H$ to adjust the aspect ratio, under vertical magnetic fields of Hartmann number $\mathrm{Ha} = 200, 1000$, with a Prandtl number $\mathrm{Pr} = 0.025$, and $2 \times 10^5 < \mathrm{Ra} \leqslant 1 \times 10^7$, encompassing the full spectrum of wall-mode flows. The selection of Ra begins at $\mathrm{Ra}_c$ for the wall mode and gradually decreases to $\mathrm{Ra}_w$, allowing for an in-depth exploration of the evolution of the wall mode with respect to the flow state and an investigation into the universal characteristics of the wall mode under varying aspect ratios and magnetic field conditions.

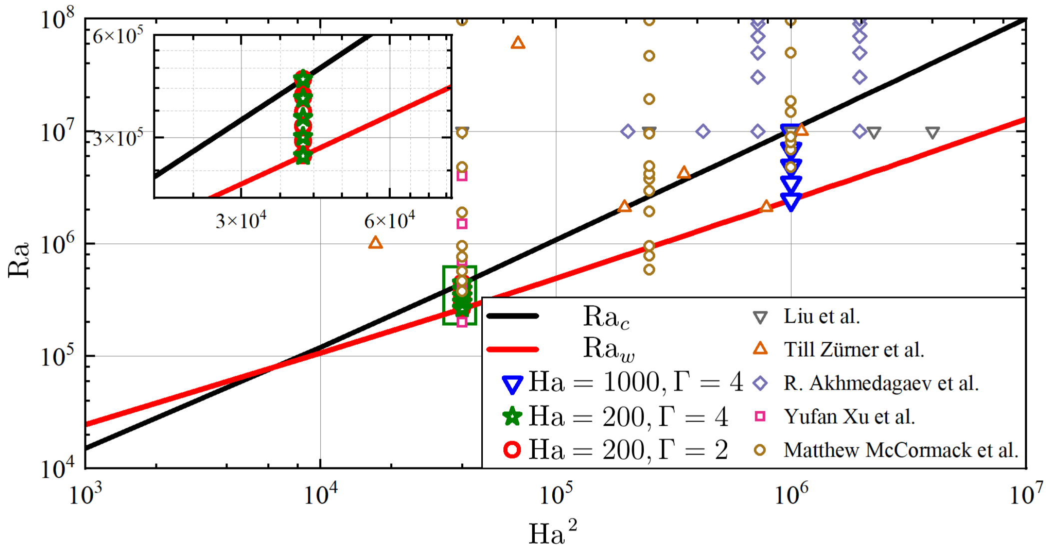


FIG. 1. The parameter range. The larger scatter points represent the parameters studied in this paper, the smaller scatter points represent the parameters in existing studies, the inverted triangles represent the research of Liu *et al*. [7] in DNS, the upward pointing triangles represent the research of Zürner *et al*. [9] in experiment, the blue diamonds represent the research of Akhmedzadev *et al*. [10] in DNS, the red square represent the research of Yufan Xu *et al*. [8] in DNS, the brown circle represent the research of McCormack *et al*. [11] in DNS.

Both analyses demonstrate that side walls amplify the intensity of thermal convection when subjected to a vertical magnetic field. Unlike natural thermal convection, which occurs in open systems, thermal convection in industrial processes generally takes place within confined containers. An analytical-numerical hybrid analysis of the particular case of a cylindrical cell reveals that side walls are responsible for the onset of thermal convection, creating a thin convective layer that adheres to the side walls, referred to as the wall mode [12].

Direct numerical simulations (DNS) conducted under conditions below the Chandrasekhar critical Rayleigh number, $\mathrm{Ra}_c$, have revealed the existence of wall-mode flow states. These wall-mode flows are characterized by circulations that closely adhere to the walls, forming two counterrotating regions on either side of the main flow. When the Rayleigh number exceeds $\mathrm{Ra}_c$, bulk cellular convection emerges [7], and near $\mathrm{Ra} \approx 5\,\mathrm{Ra}_c$, the bulk convection exhibits a drifting phenomenon around the central axis [10]. Experimental observations have also confirmed the presence of wall-mode flows [9], with multiple wall-mode flows detected by monitoring the temperature of the side walls, which is a primary characteristic of this mode. The wall-mode flow represents the initial state of thermal convection, and as Ra approaches the Busse critical $\mathrm{Ra}_w$, both experimental data and DNS have corroborated that the global Nusselt number (Nu) approaches 1 [8], thus validating the existence of the wall-mode flow state between the two critical Rayleigh numbers ($\mathrm{Ra}_c$ and $\mathrm{Ra}_w$). Under varying magnetic field strengths, the transition from wall-mode flow to bulk convection undergoes different destabilization processes. Additionally, bulk flows can coexist with the wall-mode state, sometimes manifesting as large-scale circulations (LSC) [11]. Adding a horizontal magnetic field raises the critical Ra for wall-mode flows, but when the horizontal magnetic field becomes sufficiently strong to induce contact between the relative wall-mode flows, the critical Ra decreases once again. The pattern of contact between wall-mode flows is influenced by initial conditions, which in turn affects the global Nu [13].

Currently, extensive research exists on the transition of wall-mode flow states, encompassing a wide range of parameters as shown in Fig. 1, yet the investigation of commonalities among these wall mode has largely been neglected. This study seeks to address this gap by focusing specifically on the flow characteristics inherent to the wall mode itself. The wall mode is believed to exist between two critical Ra, derived from the stability analysis of an infinite plane layer and a semi-infinite plane layer with side walls. As Ra increases, the wall mode gradually extends into the bulk, increasing the volume fraction occupied by convection. Concurrently, the global Nu of the cell also rises. However, whether it is the expansion of the wall-mode volume or the intensification of convection within the wall mode that primarily drives the increase in global Nu remains an open question, one that warrants further investigation, especially in relation to magnetic field strength and aspect ratio. Furthermore, the issue of wall-mode drift remains contentious. While numerous circulations exist in the bulk of the cell, they are relatively weak and contribute minimally to overall convective heat transfer. In most instances, these circulations are small scale, with large-scale circulations (LSC) occurring in only a minority of cases [11]. The study of bulk circulations is vital for understanding the transition of flow states, requiring a detailed quantification of circulation proportions in the bulk for deeper analysis. In light of this, this study aims to accomplish the following objectives:

(i) Investigate the drift of wall mode by monitoring the temporal variations in the temperature distribution on the wall surface;

(ii) Utilize the root-mean-square (r.m.s.) velocity to precisely delineate the circulation regions within the wall-mode flow area, and analyze the impact of varying magnetic field strengths and aspect ratios on heat transfer intensity and wall-mode volume, in conjunction with the normalized Ra;

(iii) Employ the r.m.s. shear ratio to identify the circulation regions within the wall-mode area in the velocity boundary layer and assess the proportion of bulk region circulations;

(iv) Explore the distribution characteristics of the temperature boundary layer and evaluates the potential effects of dissipation and forces on the distribution of wall-mode flows.

The outline of the paper is as follows. Section II introduces the mesh setup for the cell, as well as the governing equations. Section III presents the main results and provides a detailed analysis, while the Sec. IV offers a summary.

## II. MODEL AND FORMULATION

### A. Governing equations

This study examines the three-dimensional flow of incompressible, viscous, and electrically conducting fluid (liquid metal) with constant physical properties in a uniform vertical magnetic field. The fluid is confined within a rectangular cell, with a vertical temperature gradient between its top and bottom boundaries. Under the quasistatic approximation, we consider the magnetic Reynolds number $\mathrm{Re_m} = U\ell/\eta \ll 1$ and the magnetic Prandtl number $\mathrm{Pr_m} = \nu/\eta \ll 1$, where $U$ and $\ell$ represent the characteristic velocity and characteristic length scale, respectively, $\eta$ is the magnetic diffusivity, and $\nu$ is the kinematic viscosity.

To nondimensionalize the governing equations, we adopted the height of the square convection channel $H$, the free-fall velocity $\mathrm{U_{ff}} = \sqrt{g\alpha\Delta TH}$, the external magnetic field strength $B_0$, and the imposed temperature difference $\Delta T = T_{\mathrm{bottom}} - T_{\mathrm{top}}$ as the reference scales for length, velocity, magnetic field, and temperature, respectively. Applying the Oberbeck-Boussinesq approximation, the governing equations are derived as follows:

$$\nabla \cdot \mathbf{u} = 0 \tag{3a}$$

$$\frac{\partial \mathbf{u}}{\partial t} + \mathbf{u}\cdot\nabla\mathbf{u} = -\nabla p + \sqrt{\frac{\mathrm{Pr}}{\mathrm{Ra}}}[\nabla^2\mathbf{u} + \mathrm{Ha}^2(\mathbf{j}\times\mathbf{e_z})] + T\mathbf{e_z} \tag{3b}$$

$$\frac{\partial T}{\partial t} + \mathbf{u}\cdot\nabla T = \sqrt{\frac{1}{\mathrm{RaPr}}}\nabla^2 T \tag{3c}$$

$$\mathbf{j} = -\nabla\phi + (\mathbf{u}\times\mathbf{e_z}) \tag{3d}$$

$$\nabla^2\phi = \nabla\cdot(\mathbf{u}\times\mathbf{e_z}). \tag{3e}$$

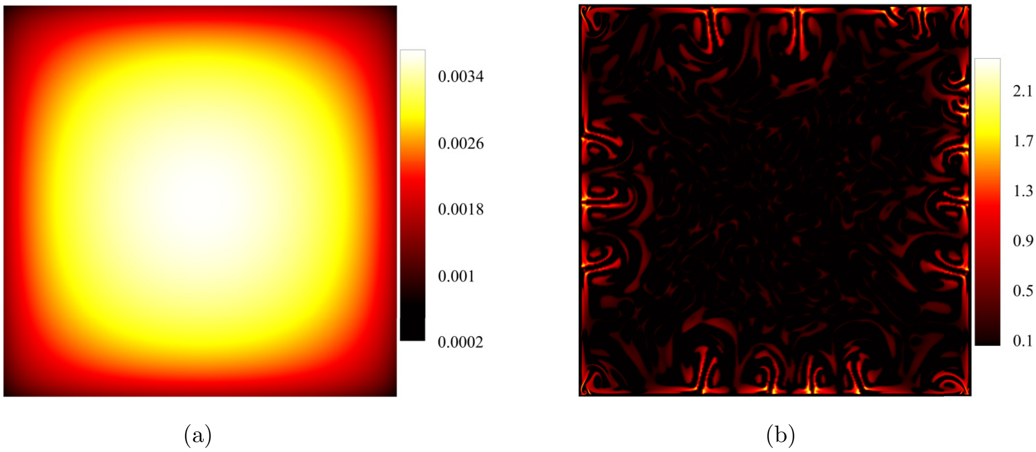


FIG. 2. Mesh quality assessment, $Z = 0$, Ha $= 1000$, $\Gamma = 4$, Ra $= 9.87 \times 10^6$. (a) Local spatial scale $\Delta l$ and (b) The ratio of the local spatial scales to the Kolmogorov scale.

In the equations $p$, $u$, $\phi$, and $T$ represent the pressure, velocity, electric potential, and temperature deviation fields, respectively. The control parameters include the Ra, the Prandtl number Pr, and the Hartmann number Ha,

$$\mathrm{Ra} = \frac{\alpha g \Delta T H^3}{\kappa \nu}, \quad \mathrm{Pr} = \frac{\nu}{\kappa} \quad \text{and} \quad \mathrm{Ha} = B_0 H \sqrt{\frac{\sigma}{\rho \nu}}.$$

In the equations, $\sigma$ represents the electrical conductivity, $\rho$ is the mass density, $\alpha$ is the coefficient of thermal expansion, $g$ is the acceleration due to gravity, $\kappa$ is the thermal diffusivity, and Pr $=$ 0.025. The top and bottom walls are maintained at constant temperatures $T = -0.5$ and $T = 0.5$, respectively. The side walls are adiabatic, satisfying $\partial T/\partial n = 0$. No-slip boundary conditions are applied on the walls, and all walls are electrically insulating, i.e., $\partial \phi/\partial n = 0$.

### B. DNS method and grid independence study

For a fluid with Pr $= 0.025$ (such as GaInSn alloy), within a certain range of Ra and Ha parameters, these equations are solved numerically. The aspect ratios of the cell, $\Gamma = L/H = W/H$ are taken as 2 and 4, respectively, where $L$ and $W$ are the lengths and widths perpendicular to the gravity direction.

A second-order finite volume method is employed on a Cartesian mesh for numerical solutions, as described by Chen *et al.* [14]. Due to computational cost constraints, we made appropriate compromises on mesh resolution. The flow was resolved on a nonuniform mesh with 2000 grid points in the horizontal direction and 300 or 350 grid points in the vertical direction. This resolution was sufficient to resolve the Hartmann, Shercliff, and thermal boundary layers, with at least 5, 15, and 20 grid points within each boundary layer, respectively. In this study, we thoroughly investigated the ratio R between the local spatial scale $\Delta l$ of the largest grid and the Kolmogorov scale $\eta_K = (\nu^3/\langle\varepsilon\rangle_{V,t})^{1/4}$, calculated based on the mean dissipation rate $\langle\varepsilon\rangle_{V,t}$, i.e., R $= \Delta l/\eta_K$, where $\langle\cdot\rangle_{V,t}$ represents the time and volume average and $\varepsilon = 2\sqrt{\mathrm{Pr}/\mathrm{Ra}} S_{ij} S_{ij}$. It's found that in the most extreme cases, this ratio was below 3, and in most simulations, the ratio was even below 2. Here, $\langle\varepsilon\rangle$ represents the time-averaged viscous dissipation. According to Vílchez [15], the local spatial scale $\Delta l$ is defined as the cube root of the cell volume, i.e., $\Delta l = (\Delta x \Delta y \Delta z)^{1/3}$, where $\Delta x$, $\Delta y$, $\Delta z$ represent the local grid sizes in the *x, y, z* directions, respectively. Figure 2(a) shows the local spatial scale $\Delta l$ at midheight, with refinement at the boundaries, resulting in a larger $\Delta l$ in the center compared to the edges. Figure 2(b) illustrates the ratio R between the local spatial scale and the Kolmogorov scale, with higher R values in the core region of the wall-mode flow, yet still not exceeding 3. Both figures in Fig. 2 correspond to the case with $\mathrm{Ha} = 1000$, $\Gamma = 4$, and $\mathrm{Ra} = 9.87 \times 10^6$, which is the most demanding scenario for mesh requirements. Further analysis indicates that changes in mesh resolution did not qualitatively or quantitatively affect the flow state or alter the Nu of the cell. Therefore, the mesh used in this study is sufficient in terms of both global variables and local spatial scales.

## III. RESULT

### A. Drift of wall mode

In magnetohydrodynamics Rayleigh-Bénard convection (MHD-RBC), when the magnetic field is sufficiently strong, thermal convection in the bulk adheres to the side walls, resembling the behavior observed in rotating Rayleigh-Bénard convection (RRBC) [16]. Similarly, when the rotational angular velocity reaches a sufficiently high threshold, the thermal convection also adheres to the side walls. It is well established that the wall-mode flow in RRBC drifts around the central axis of the cell, and numerous studies have explored the relationship between its drift velocity, temperature difference, and rotational speed [17]. However, a debate persists regarding whether the wall mode in magnetic Rayleigh-Bénard convection exhibits drift.

Akhmedagaev *et al.* [10] observed the drift phenomenon of the wall mode in the vertical velocity field at the middle height of a cylindrical cell during DNS, but the Rayleigh number they observed was considerably higher than $\mathrm{Ra}_c$. Zürner *et al.* [9] monitored the temperature distribution on the side walls in experiments, while Liu *et al.* [7] and Xu *et al.* [8] made intuitive assessments of the velocity field through DNS, and none detected any drift of the wall mode. Based on current research findings, it can be inferred that although the noselike portion of the wall mode may oscillate, its core remains firmly adhered to the side walls, without exhibiting any drift.

In this study, for the series of cases with $\mathrm{Ha} = 1000$ and $\Gamma = 4$, the temperature distribution on the sidewall was monitored over a period of 100 dimensionless time units to observe its temporal variation, which is significantly longer than the 50 dimensionless time units monitored by Zürner *et al.* [9]. Akhmedagaev *et al.* [10] observed multiple drifts within 100 dimensionless time units, which were not detected in the present study. The temperature distribution on the sidewall serves as an indicator of the position of the core region of the wall-mode flow, a method commonly applied in the study of RRBC. Figure 3 presents five different Ra within the wall-mode Ra range, where the red region represents the hot ascending flow area and the blue region denotes the cold descending flow area. The positions of these regions remained unchanged over the course of 100 dimensionless time units, suggesting that the wall mode in MHD-RBC does not exhibit drift.

The Coriolis force in RRBC promotes latitudinal motion, whereas the Lorentz force in MHD-RBC tends to suppress it. This is akin to the suppression of large-scale circulation (LSC) oscillations under a vertical magnetic field, as observed by Lim *et al.* [18].

### B. Delineation of the wall-mode region

This article quantitatively investigates the heat transfer and flow patterns of the wall mode in MHD-RBC by partitioning the cell into wall-mode and bulk regions. In previous studies, a fixed value is commonly used to delineate the wall-mode region. Liu *et al.* [7] employed a square region with a fixed side length to separate the central and wall-mode regions in numerical simulations of a square cell. Zhang *et al.* [16] used a circular region with a fixed radius to define corresponding areas in their study of RRBC in a cylindrical cell.

While the fixed value method for delineating the wall-mode region can qualitatively indicate whether the flow and heat transfer within the wall-mode region dominate, it has limitations in quantitative analysis. Specifically, it fails to accurately assess the effects of variations in magnetic field strength and adjustments to the aspect ratio of the cell on the heat transfer intensity and volume of the wall mode. In earlier studies of MHD wall mode, the simplicity and speed of the fixed value

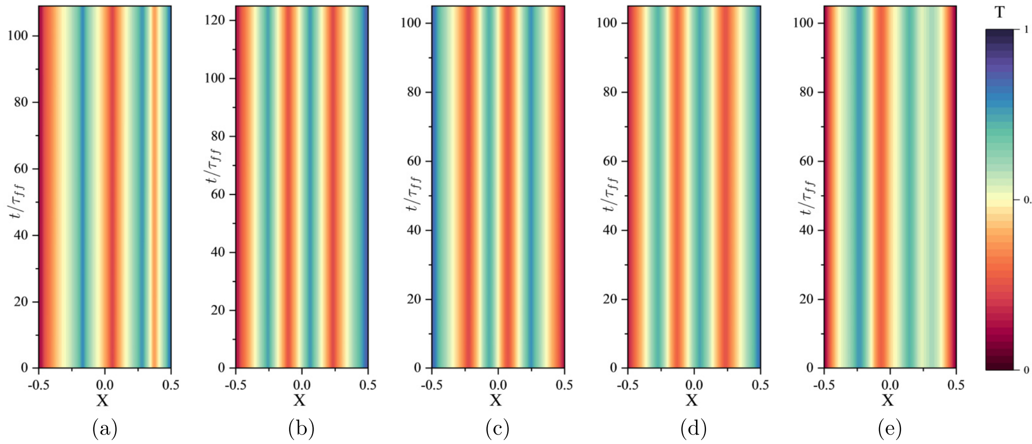


FIG. 3. The temperature distribution on the side wall changes with dimensionless time. The Horizontal coordinate represents the position on a line with $Y = -0.5$, $Z = 0$, and the vertical coordinate represents the dimensionless time. The Ra decreases from left to right, (a) $9.87 \times 10^6$, (b) $6.97 \times 10^6$, (c) $4.92 \times 10^6$, (d) $3.47 \times 10^6$, (e) $2.45 \times 10^6$. Ha = 1000, $\Gamma = 4$.

partitioning method made it a convenient tool for identifying the overall state of wall-mode flow. However, as our research advances, it has become evident that a more refined method for delineating wall mode is needed—one based on the flow state itself, so as to more accurately capture the dynamic characteristics of wall mode.

In this study, the partitioning of regions is based on the flow state, with the wall-mode region characterized by rapid flow velocities in the $z$ direction, where $U_z$ significantly exceeds that in the central region. Isolating the high-velocity flow area as the wall-mode region more accurately reflects the nature of the flow, thereby facilitating a better understanding of the heat transfer mechanisms in wall-mode flow states. The variance of the vertical velocity $U_z$ captures the average fluctuation of $U_z$, and regions where the fluctuations of $U_z$ exceed the range of its variance can be considered distinct ascending and descending flow areas. Consequently, the delineation of the wall mode adopts the region defined by

$$|U_z| \geqslant \sqrt{\left(U_z^2\right)_V}, \tag{4}$$

where $(U_z^2)_V$ represents the volume average of $U_z^2$, a method employed by Zhang *et al.* [19] to study the coverage rate of plumes in the boundary layer. It is also employed by Zhu *et al.* [20] to study the flows in the bulk. In studies related to the partitioning of flow regions, the root-mean-square (r.m.s.) velocity provides a convenient means to distinguish the primary flow areas.

The ascending and descending flows within the wall mode are distinctly observable in Fig. 4, which presents the wall-mode region delineated by the r.m.s. of velocity. The counterflow on both sides of the main stream is also clearly visible, as previously noted by Liu *et al.* [7] through vertical velocity isosurface.

To validate the reliability of this partitioning method, this study considers both the intuitive velocity distribution and the statistical kinetic energy fraction. Figure 5(b) extracts the velocity distribution along the black dashed line in Fig. 5(a), which presents the isosurface of the vertical velocity $U_z$ at midheight with Ha = 1000, $\Gamma = 4$, and Ra = $9.87 \times 10^6$. The red and blue regions distinctly represent the ascending and descending flows, respectively; the red portion indicates the velocity distribution of the bulk, while the black points represent the velocity distribution of the wall-mode region. The black points section occupies the high-speed flow area, clearly delineating the wall-mode region, thus demonstrating that the region partitioning method based on the r.m.s.

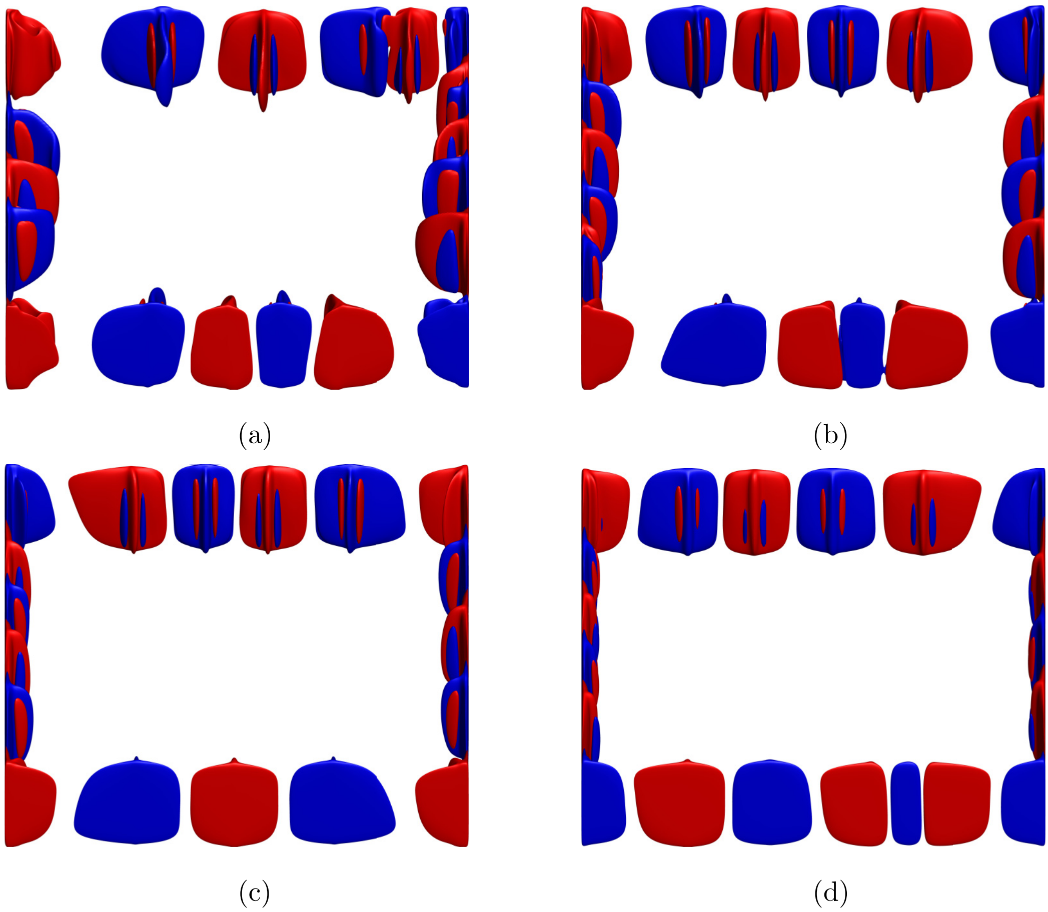

FIG. 4. The wall-mode region delineated by $|U_z| \geqslant \sqrt{(U_z^2)_V}$ (Ha = 1000 and $\Gamma = 4$) three-dimensional (3D) velocity diagram observed from the front-top position, where the red area represents the ascending flow and the blue area represents the descending flow. (a) Ra = $9.87 \times 10^6$, (b) Ra = $6.97 \times 10^6$, (c) Ra = $4.92 \times 10^6$, and (d) Ra = $3.47 \times 10^6$.

of velocity is viable. The vertical velocity is compressed near the walls, with the high-speed flow region on the left corresponding to the descending flow, and that on the right to the ascending flow. Meanwhile, the bulk exhibits only slight flow fluctuations.

The partitioning method is validated using the proportion of kinetic energy. $(U_{zw}^2)_V$ represents the volume integral of the kinetic energy in the $z$ direction within the wall-mode region, while $(U_z^2)_V$ represents the volume integral of the kinetic energy in the $z$ direction over the entire cell. The ratio $(U_{zw}^2)_V/(U_z^2)_V$ can reflect the proportion of kinetic energy in the wall-mode region relative to the global kinetic energy, as shown in Fig. 6(a), showing a decrease in this fraction as Ra increases, indicative of a growing temperature difference leading to an increasing prevalence of low-velocity flow in the bulk. However, within the entire Ra number range of the wall mode, the kinetic energy proportion of the wall-mode region exceeds 92%. This study quantitatively confirmed through kinetic energy analysis that the wall mode is the primary flow region, which aligns with the qualitative observations made by Liu *et al.* [7] and Xu *et al.* [8]. Additionally, this further validates the efficacy of the partitioning method utilized in this research.

The kinetic energy fraction in the wall-mode region decreases with increasing Ra in Fig. 6(a), reflecting an increasing vertical flow in the bulk. Although these flows still occupy a small propor-

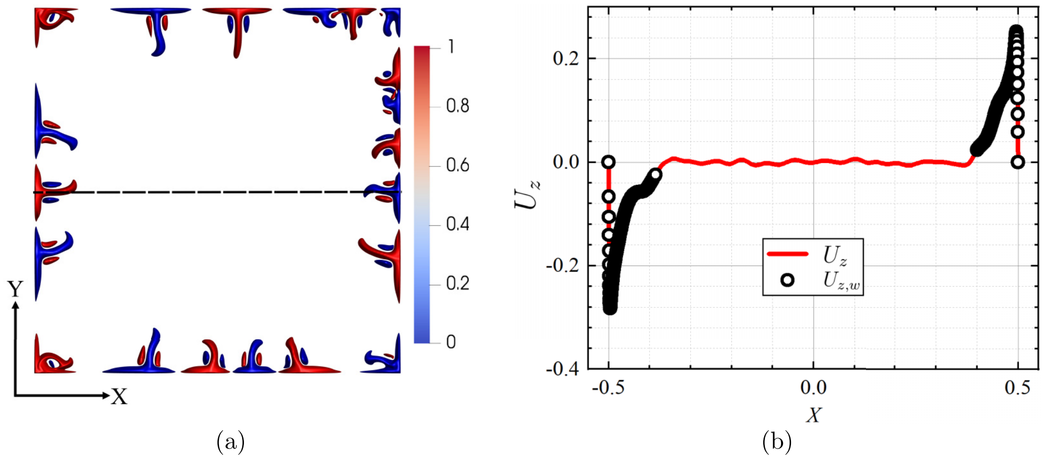


FIG. 5. Validation of wall mode partitioning method. (a) Vertical velocity $U_z$ contour plot in the $xy$ plane at the $Z = 0$ of the wall-mode region delineated by $|U_z| \geqslant \sqrt{(U_z^2)_V}$ (Ra $= 9.87 \times 10^6$, Ha $= 1000$, and $\Gamma = 4$) where the black dashed line is the horizontal line at the $Y = 0$. (b) The distribution of the vertical velocity $U_z$ along the black dashed line in the left figure, which exactly includes the complete ascending and descending flows at the left and right ends (red line), the black points denotes which of the wall-mode region.

tion, their increasing trend reflects the transition of wall-mode flow states towards bulk convection. McCormack *et al*. [11] studied this transition process from a stability perspective, and this study points out that this transition process spans the entire wall-mode flow state, with the flow in the central region gradually increasing. Figure 6(b) depicts the variation in the volume fraction of the wall-mode region, distinguished by the r.m.s. velocity, with a normalized horizontal axis that enables the comparison of wall-mode flow states under different magnetic fields; all three series of wall-mode volume fractions increase with the Ra, exhibiting similar rates of change. The volume ratio under strong magnetic fields is significantly smaller, reflecting the magnetic field's inhibitory effect on the flow. A decrease in the aspect ratio increases the wall-mode volume ratio; the two series of cases at Ha $= 200$ differ by a factor of 2 in aspect ratio, yet the wall-mode fraction does not differ by a factor of 2. The reduction in aspect ratio not only compresses the bulk region but also compresses the volume of the wall-mode region.

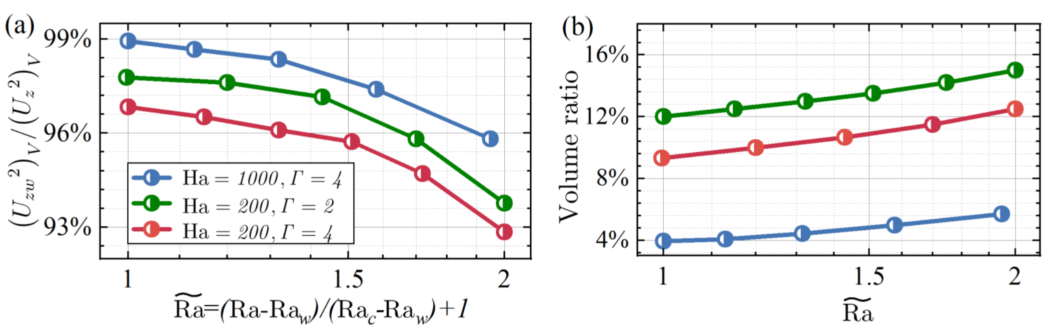


FIG. 6. (a) The vertical kinetic energy ratio of the wall mode $(U_{zw}^2)_V/(U_z^2)_V$. (b) The volume ratio of the wall mode (the ratio of the volume of the region where $|U_z| \geqslant \sqrt{(U_z^2)_V}$ to the total volume).

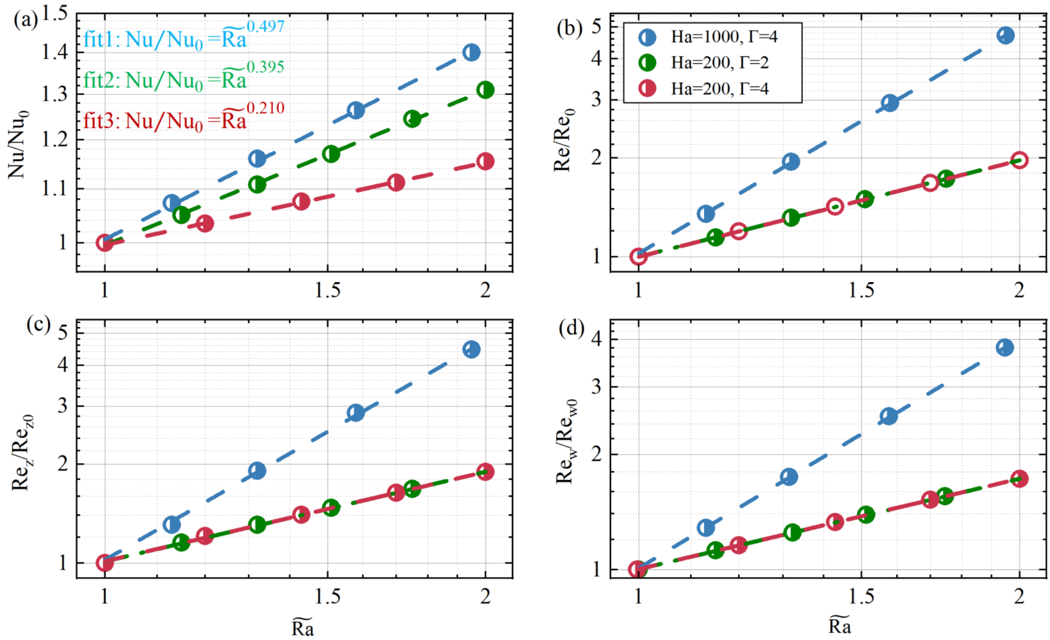


FIG. 7. (a) The variation of Nu with $\tilde{\mathrm{Ra}}$. (b) The variation of Re with $\tilde{\mathrm{Ra}}$. (c) The variation of $\mathrm{Re}_z$ with $\tilde{\mathrm{Ra}}$. (d) The variation of $\mathrm{Re}_w$ with $\tilde{\mathrm{Ra}}$. The $Y$ axis quantities have been normalized using the values at $\mathrm{Ra} = \mathrm{Ra}_w$. These values are given the subscript 0. The dashed line is the fitting line through the points.

### C. Flow and heat transfer characteristics

The global Nu and Reynolds numbers (Re) are displayed in Fig. 7, respectively. The definition of the Nu and Re are given by

$$\mathrm{Nu} = 1 + \sqrt{\mathrm{RaPr}}\langle U_z T\rangle_{V,t}, \quad \mathrm{Re} = \sqrt{\mathrm{Ra}/\mathrm{Pr}}U_{\mathrm{rms}}, \tag{5}$$

with $U_{\mathrm{rms}} = \sqrt{\langle u_i^2\rangle_{V,t}}$ being the r.m.s. velocity, where $\langle\cdot\rangle_{V,t}$ represents the time and volume average within the cell. The Ra has been normalized to facilitate a comparative analysis across varying magnetic field strengths and aspect ratios. Similarly, both Nu and Ra have undergone normalization. In examining the relationship between Ra and Nu, a clear trend of proportionality between Nu and increasing Ra emerges. By applying a fitting procedure, the scaling law $\mathrm{Nu} \sim \mathrm{Ra}^{\beta}$ was derived, with the value of $\beta$ provided in Table I. The table also includes the scaling law established by Akhmedagaev *et al.* [10] for $\mathrm{Ra} \geqslant \mathrm{Ra}_c$, characterizing the cell convection state, which is the next convection state after wall mode with the increase of Ra. Notably, the value of $\beta$ in the wall-mode state is significantly smaller than that observed in the cell convection state, a finding corroborated by Teimurazov *et al.* [21] in the context of RRBC. To visually represent these results, the corresponding scaling law diagram was plotted with normalized $\tilde{\mathrm{Ra}}$ and Nu as the axes, as illustrated in Fig. 7

TABLE I. Scaling law of Nu.

| | $\mathrm{Ha} = 1000, \Gamma = 4$ | $\mathrm{Ha} = 200, \Gamma = 4$ | $\mathrm{Ha} = 200, \Gamma = 2$ |
|---|---|---|---|
| $\beta$ | 0.23931 | 0.28157 | 0.53353 |
| | $\mathrm{Ha} = 0, \Gamma = 1$ | $\mathrm{Ha} = 850, \Gamma = 1$ | $\mathrm{Ha} = 1400, \Gamma = 1$ |
| $\beta$ [10] | 0.298 | 0.513 | 0.574 |

a, where $\tilde{\mathrm{Ra}} = (\mathrm{Ra} - \mathrm{Ra}_w)/(\mathrm{Ra}_c - \mathrm{Ra}_w) + 1$ and $\mathrm{Nu}_0$ is the Nu of case which $\mathrm{Ra} = \mathrm{Ra}_w$, the subscript 0 later is similar. When the convective onset is at $\mathrm{Ra}_w$, $\mathrm{Nu}_0 = 1$. However, in actual DNS, the difference between Nu and 1 is within about 5%. For cases in the same series, the same grid is used. By adopting $\mathrm{Nu}/\mathrm{Nu}_0$, the slight systematic errors can be eliminated.

Within the wall-mode range, the variation of Nu remains relatively constrained, showing no substantial increase. Conversely, the Re rises with increasing Ra, indicating a positive correlation between convective heat transfer intensity and flow strength. Interestingly, changes in the aspect ratio significantly influence the growth of Nu, yet this impact is not mirrored in the growth rate of Re. The effect of the magnetic field on both Nu and Re, however, appears consistent; under strong magnetic fields, the growth rates of both parameters increase markedly.

This disparity in how magnetic field strength and aspect ratio influence global parameters necessitates a deeper examination of the flow dynamics to elucidate the underlying causes. As discussed in various Rayleigh-Bénard convection (RBC) studies, such as Zhang *et al.* [16], the Re and Nu numbers aligned with heat transfer direction often exhibit similar trends. This observation suggests that the study of wall modes can focus on the vertical Reynolds number, $\mathrm{Re}_z$, defined as $\mathrm{Re}_z = \sqrt{\mathrm{Ra}/\mathrm{Pr}}U_{z,\mathrm{rms}}$. Figure 7(c) illustrates the growth law of the global $\mathrm{Re}_z$ within the cell, demonstrating no significant deviation from the growth law of Re presented in Fig. 7(b). This similarity underscores that the global vertical $\mathrm{Re}_z$ governs heat transfer. Nevertheless, the variation pattern of $\mathrm{Re}_z$ diverges from that of heat transfer intensity, suggesting the necessity for a detailed investigation into the impact of the wall-mode flow structure.

The Reynolds number in the wall-mode region, $\mathrm{Re}_w = \langle \mathrm{Re} \rangle_{W,t}$, where $\langle \cdot \rangle_{W,t}$ denotes the time and volume average within the wall-mode region, as depicted in Fig. 7(d), reveals a growth trajectory akin to that of the global $\mathrm{Re}_z$ and the overall Re. This finding reinforces the identification of the wall-mode region as the pivotal zone of the flow, dictating its primary characteristics. Furthermore, the negligible contribution of horizontal flow to the Re underscores its insignificance in triggering anomalies within the Re. This observation aligns with Akhmedagaev *et al.* [10], who asserted that the flow in the wall-mode region is predominantly vertical, serving as the principal driver of heat transfer. The analysis conducted by Zhang *et al.* [19], focusing on convective heat transfer intensity in RBC studies, offers further insights that complement this research. These findings harmonize with the validated methodology for partitioning the wall-mode region established in this study.

The convective heat transfer intensity,

$$J_{c,w} = \sqrt{\mathrm{RaPr}}\langle U_z T \rangle_{W,t}, \tag{6}$$

and the diffusive heat transfer intensity,

$$J_{d,w} = -\frac{\partial \langle T \rangle_{W,t}}{\partial z}, \tag{7}$$

within the wall-mode region are illustrated in Fig. 8. In Fig. 8(b), $J_{d,w}$ exhibits a decreasing trend with increasing Ra, contrasting with the global Nu of the cell. Notably, the slope of this decrease mirrors the slope of the increase in the global Nu, reflecting the opposing tendencies of convective and diffusive heat transfer. Conversely, in Fig. 8(a), $J_{c,w}$ retains a growth pattern similar to that of Re, affirming the direct correlation between convective heat transfer and flow intensity.

In summary, strong magnetic fields enhance heat transfer intensity, accompanied by an increase in flow intensity. However, variations in the aspect ratio neither influence flow intensity nor alter convective heat transfer intensity within the wall-mode region. When considering Fig. 6, the rationale becomes evident: reducing the aspect ratio compresses the intermediate region, allocating more cell volume to convective heat transfer. This expansion of the wall-mode region volume accounts for the higher global Nu observed in convection cells with smaller aspect ratios.

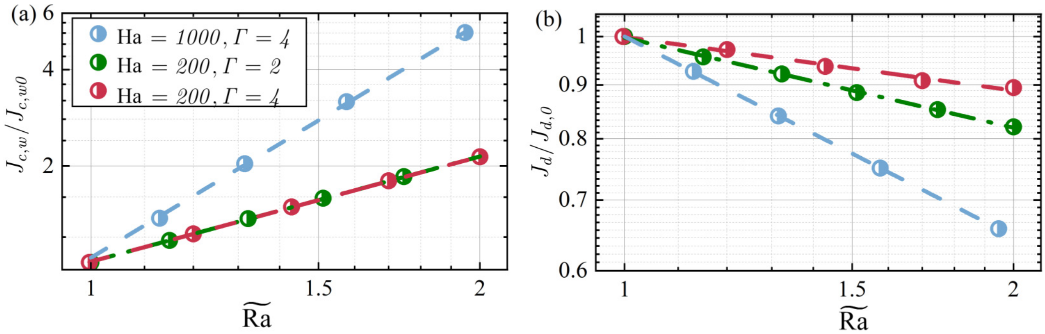


FIG. 8. (a) The variation of normalized convective heat transfer in the wall-mode region $J_{c,w}$ with the normalized Ra. (b) The variation of normalized diffusive heat transfer in the wall-mode region $J_{c,w}$ with the normalized Ra. (The dashed line is the fitting line.)

### D. Circulation in the bulk

The primary flow and heat transfer in the wall mode flow state are concentrated near the side walls, with the flow forming circulatory patterns closely adhering to these walls, as detailed by Liu *et al*. [7]. Nonetheless, a notable amount of circulation persists in the cell's bulk, as depicted in Fig. 9(a) that is composed of a streamline diagram and an isosurface divided by the root-mean-square (r.m.s.) velocity. From the streamline diagram, it can be observed that there is a significant amount of flow in the bulk region. However, the velocity of these flows are very small, and they contribute almost nothing to the convective heat transfer of the cell. These streamlines are the result of time averaging and do not change in multiple adjacent time steps, indicating that they are not caused by numerical noise. This observation is consistent with the findings by McCormack *et al*. [11], who also observed the bulk circulation.

They highlighted that during the transition from wall mode to cell convection, the strength of the magnetic field influences the initiation of thermal convection within the bulk. Understanding bulk flow is thus critical for analyzing flow state transitions. This study presents a shear ratio cloud map within the velocity boundary layer, effectively distinguishing the high-velocity wall circulation from

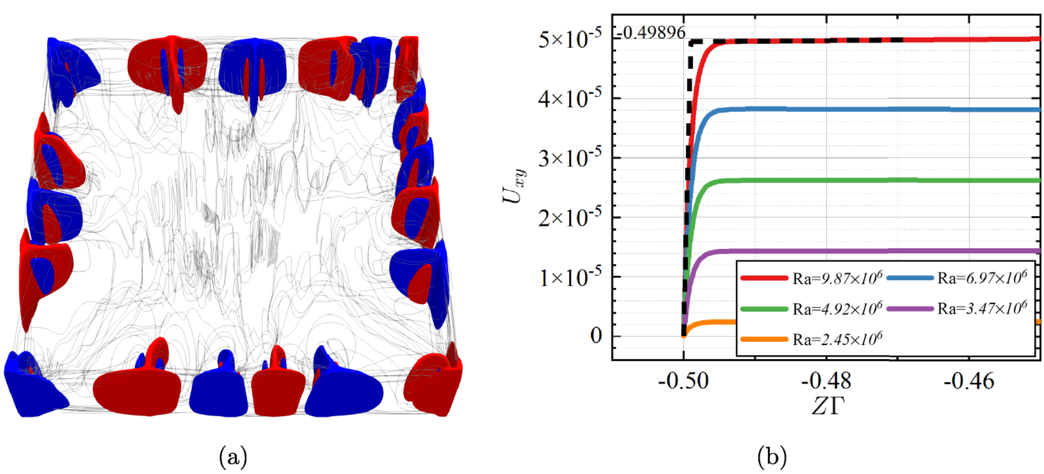


FIG. 9. (a) The wall-mode region with streamline in the bulk (time-averaged Ha = 1000, 9.87 × $10^6$, and $\Gamma = 4$). (b) Distribution of $U_{xy}$, averaged over horizontal planes along $z$ direction.

TABLE II. Dimensionless velocity boundary layer thickness.

| Ha = 1000, Γ = 4 | Ha = 200, Γ = 2 | Ha = 200, Γ = 4 |
|---|---|---|
| 0.00104 | 0.00519 | 0.005 |

the low-velocity core circulation. The r.m.s. method is employed for regional division, analogous to the approach applied to delineate the wall-mode region.

The variation in the averaged horizontal velocity with respect to $Z$ throughout the bulk is depicted in Fig. 9(b), where the horizontal velocity is defined as $U_{xy} = \sqrt{U_x^2 + U_y^2}$. The thickness of the velocity boundary layer is clearly represented in Fig. 9(b) by the intersection of the two asymptotic dashed lines, a method employed by Pandey [22] in his investigation of the boundary layer thickness in RBC. From Fig. 9(b), it is evident that neither variations in the Ra nor changes in the aspect ratio affect the thickness of the velocity boundary layer. Rather, this thickness is predominantly determined by the strength of the magnetic field. Table II provides a summary of the velocity boundary layer thickness for three distinct series of computational cases, all of which closely approximate the thickness of the Hartmann boundary layer, calculated as $\delta_{\mathrm{Ha}} = H/\mathrm{Ha}$. Thus, the magnetic field emerges as the predominant factor shaping the velocity gradient at the boundary.

The shear rate contour plot of the velocity boundary layer, presented in Fig. 10(a), clearly demonstrates that the shear ratio in the edge regions is markedly higher than in the central areas. These red regions with elevated shear rates correspond to the continuity of the wall circulation, while the central regions, exhibiting lower shear rates, are part of the core circulation. In Fig. 10(b), the r.m.s. method is employed to delineate regions, defined by $\tau = |\frac{\partial U_x}{\partial z} + \frac{\partial U_y}{\partial z}| > \sqrt{(\tau^2)_v}$, resulting in the shear contour plot of the central region, where the dark red areas, representing wall circulation, are identified. This partitioning method has been validated in previous sections and, as evident from the contour plots, proves to be highly effective.

The area integral of the shear rate across the velocity boundary layer, as it increases with Ra, is shown in Fig. 11(a). This reflects the enhancement of circulation intensity with rising Ra, mirroring the growth of Re throughout the cell. The strength of the magnetic field plays a significant role in amplifying the circulation intensity, while the aspect ratio has no discernible impact on this intensity.

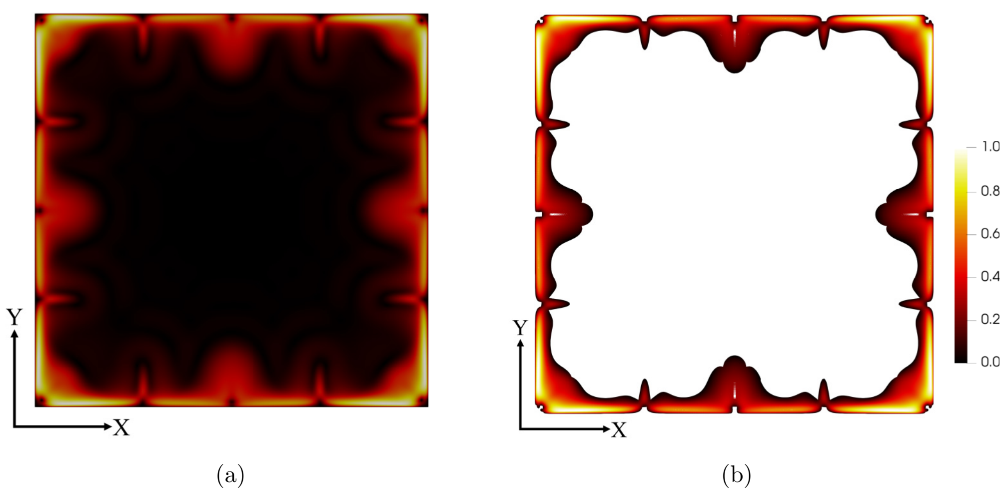


FIG. 10. Shear rates of $xy$ plane on bottom boundary layer. (The distance from the bottom plate use the data in Table II. Ha = 200, Γ = 2, Ra = $4.445 \times 10^5$.) (a) Shear rates on the velocity boundary layer and (b) Shear rates of the wall mode region on the volocity boundary layer.

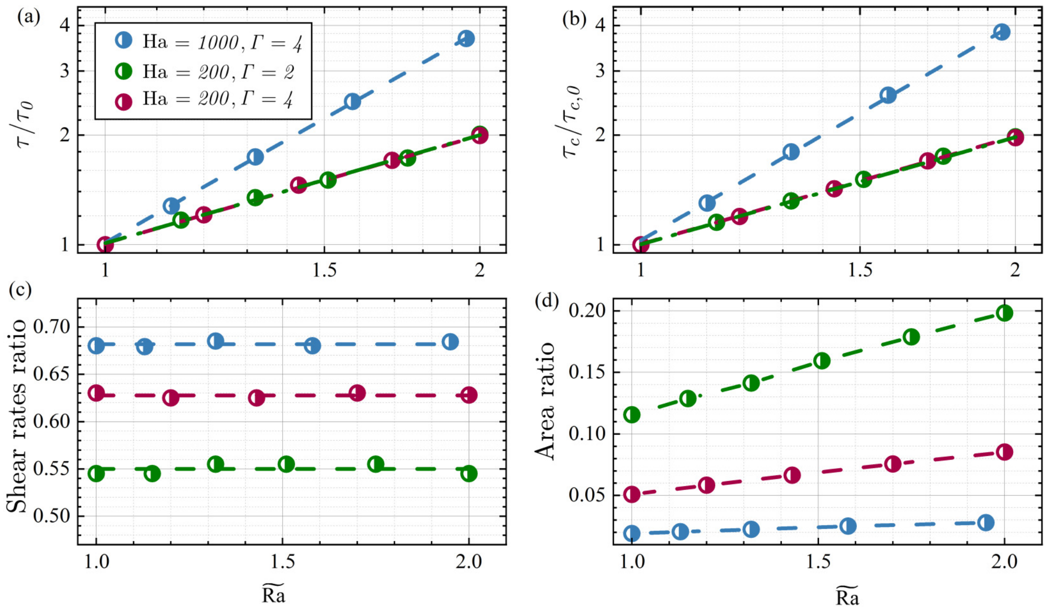


FIG. 11. (a) The shear ratio. (b) The shear stress in the bulk. (c) Proportion of the body circulation. (d) Area fraction of the wall circulation (the dashed line is the fitting line).

Figure 11(b) illustrates the area integral of shear rate within the bulk, which increases in parallel with the global shear rates. Both the body circulation in the bulk and the wall circulation grow proportionally, with the body circulation occupying a substantial fraction of the system throughout the wall-mode state.

The proportion of the overall circulation occupied by the body circulation in the bulk is quantified in Fig. 11(c), that the body circulation consistently accounts for more than 50% of the total circulation across the entire range of Ra. This indicates that although the flow in the body region is weaker and its heat transfer is negligible, the total volume of body circulation always constitutes a major part of the total circulation. Figure 11(d) illustrates the area fraction of the velocity boundary layer occupied by wall circulation, which follows a similar variation pattern to the volume fraction of the wall mode. The magnetic field suppresses the extent of wall circulation, and a decrease in the aspect ratio significantly increases the area fraction of wall circulation. Regardless of whether the magnetic field is strong or weak, the proportion of wall circulation increases with Ra. This also suggests that during the transition from the wall-mode state to the bulk convection state, there must be an extension of the wall-mode region towards the bulk. This complements the research on flow state transitions by McCormack *et al*. [11].

### E. Thermal boundary layer

The thickness of the velocity boundary layer is not influenced by the Ra and is solely related to the Hartmann boundary layer, as depicted in Fig. 9(b). In contrast, the thickness of the thermal boundary layer is jointly affected by the temperature difference, magnetic field, and aspect ratio, and even exhibits significant differences at various locations.

In the wall-mode, within the impact zones of the ascending-flow and descending-flow regions, a temperature boundary layer exists. Figure 12 vividly displays the velocity contour in the vicinity of the side wall. The position demarcated by the black dashed line denotes the core regions of both the ascending flow and the descending flow. In this figure, the blue-colored portion represents the descending flow, while the red-colored portion stands for the ascending flow. Specifically, the areas

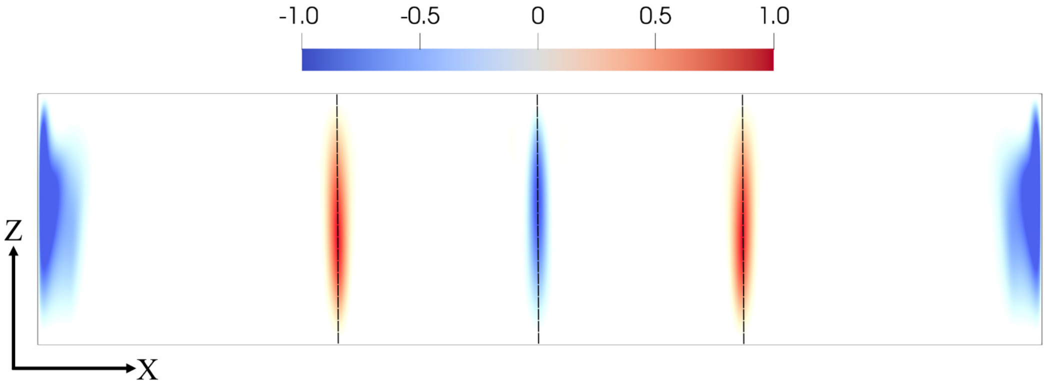


FIG. 12. Vertical velocity $U_z$ contour plot in the $xz$ plane at the $Y = 0.48$, the black dashed line reflects the core position of the wall mode (Ha = 200, $\Gamma = 4$, and Ra = $4.45 \times 10^5$).

where the ascending flow approaches the top plate and the descending flow approaches the bottom plate are defined as the impact regions. Conversely, the areas where the ascending flow approaches the bottom plate and the descending flow approaches the top plate are referred to as the eject regions. Figure 13(a) presents the temperature distribution in the $z$ direction. This distribution is obtained by averaging the temperature values over multiple descending-flow regions. Simultaneously, the temperature distributions of multiple ascending-flow regions are averaged in the reverse direction. The purpose of this operation is to acquire the average temperature distribution within the impact zone. As a result, the left-hand part of Fig. 13(a) corresponds to the impact region. This detailed analysis of the flow and temperature distributions provides crucial insights into the complex physical

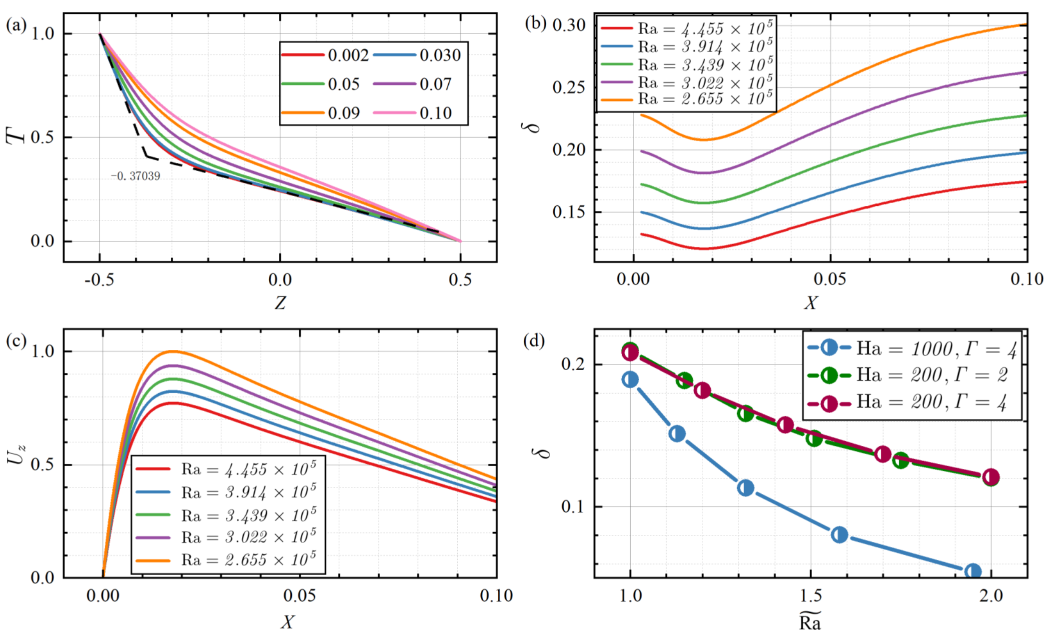


FIG. 13. (a) Temperature distribution along the $z$ axis in the wall-mode descending flow region (different colored lines represent the distances from the side edge). (b) Temperature boundary layer thickness in the impact region. (c) Distribution of $U_z$ in the wall-mode region. (d) Thermal boundary layer thickness.

processes occurring within the wall mode, enabling a more in-depth understanding of the underlying mechanisms.

The temperature distribution along the $z$ axis in the wall-mode regions is illustrated in Fig. 13(a) with $\mathrm{Ha} = 200$, $\Gamma = 4$, and $\mathrm{Ra} = 4.45 \times 10^5$, where the legend represents the distance from the side wall. The turning point here is the intersection of two asymptotic dashed lines, and this intersection reflects the thickness of the temperature boundary layer, which is also employed by Pandey [22]. The temperature distribution in the Fig. 13(a) can be observed that the farther away from the side wall, the thicker the thermal boundary becomes, until the temperature distribution turns into a straight line. In the gap between the ascending and descending flows, as well as in the bulk region, the $z$-direction temperature distribution is a straight line. This indicates that the temperature boundary layer only exists in the impact region, where there is significant heat diffusion, as mentioned by Ronald [23], when the fluid flows at a high velocity, the temperature gradient mixes rapidly, making it impossible to observe a distinct thermal boundary layer. The variations in the temperature boundary layer in the impact region will be further studied.

The variation of the thermal boundary layer obtained by the same method with Fig. 13(a) in the impact zone for the $\mathrm{Ha} = 200$, $\Gamma = 4$ series of cases is illustrated in Fig. 13(b), with the horizontal axis representing the distance from the measurement point to the sidewall. The minimum value of the red line in Fig. 13(b) corresponds to the boundary layer thickness obtained from the example asymptotic dashed lines in Fig. 13(a). As the wall mode extends towards the bulk region, the thickness of the temperature boundary layer first decreases and then increases. Additionally, a larger Ra compresses the thickness of the temperature boundary layer. It is easy to understand that a greater convective intensity brings the impact zone closer to the boundary. Figure 13(c) shows the vertical velocity distribution in the wall-mode region, which averages both the ascending and descending flows. Combining Fig. 13(b), it can be observed that the thinnest position of the boundary layer coincides with the position where the wall mode velocity is the fastest. At the core of the wall mode where the $U_z$ is the greatest, the temperature boundary layer is the thinnest, and in the proboscis region of the wall mode, the temperature boundary layer is the thickest.

The thickness of the temperature boundary layer at its thinnest point are selected in Fig. 13(d) to demonstrate how the temperature boundary layer varies with Ra. A stronger temperature difference drive leads to greater flow intensity within the cell, which in turn makes the temperature boundary layer thinner. The variation of the temperature boundary layer thickness is inversely related to the Re; the temperature boundary layer in the wall-mode region is suppressed by the magnetic field and is not affected by the aspect ratio. Summarizing previous research findings, it can be observed that the enhancement of the magnetic field and the reduction of the aspect ratio both increase the global Nu of the cell. The magnetic field strengthens the heat transfer intensity in the wall-mode region, which is reflected in the enhancement of the circulation intensity, and simultaneously compresses the thickness of the temperature boundary layer. The reduction of the aspect ratio compresses the volume of the bulk, increasing the volume available for effective heat transfer, which is positive to enhancing heat transfer. However, changes in the aspect ratio do not alter the heat transfer intensity in the wall-mode region.

### F. Dissipation and force balance

The wall mode is a flow attached to the side wall, with a noselike projection extending towards the central region, flanked by reverse flows on both sides. Liu *et al.* [7] first discovered this flow phenomenon, with the core of the reverse flow located approximately at a position $3.47\delta_{\mathrm{sh}}$ away from the wall surface, where $\delta_{\mathrm{sh}}$ is the thickness of the Shercliff boundary layer, calculated by $\delta_{\mathrm{sh}} = H/\sqrt{\mathrm{Ha}}$. However, they did not reveal the cause of this reverse flow. In this section, taking $\mathrm{Ha} = 200$, $\Gamma = 4$, $\mathrm{Ra} = 4.45 \times 10^5$ as an example, we attempt to analyze the wall mode and its reverse flows on both sides from the perspectives of dissipation and force.

The momentum equation is decomposed into terms, and the controlling forces of MHD-RBC (inertial force, Lorentz force, pressure gradient, viscous force, and buoyancy) are expressed in

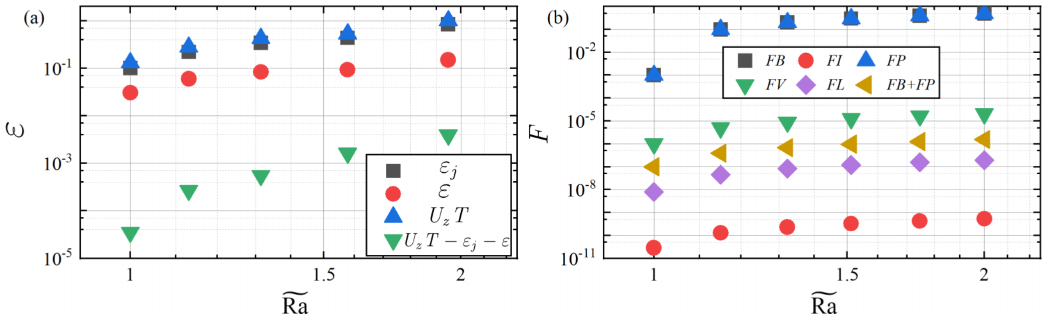


FIG. 14. (a) Dissipation balance (Ha = 200, Γ = 4). (b) Force balance (the magnitude of the force vector, Ha = 200, Γ = 4).

dimensionless form as follows:

$$\mathbf{F_I} = -(\mathbf{u}\cdot\nabla)\mathbf{u}, \quad \mathbf{F_B} = \theta\mathbf{e_z}, \quad \mathbf{F_p} = -\nabla p, \quad \mathbf{F_V} = \sqrt{\frac{\mathrm{Pr}}{\mathrm{Ra}}}\nabla^2\mathbf{u}, \quad \mathbf{F_L} = \mathrm{Ha}^2\sqrt{\frac{\mathrm{Pr}}{\mathrm{Ra}}}(\mathbf{j}\times\mathbf{e_b}).$$

Taking the dot product of the dimensionless velocity u with the dimensionless momentum equation, and gathering all the divergence terms together, we perform a volume integration over the entire equation. This yields the integral form of the dimensionless kinetic energy equation:

$$\frac{\partial}{\partial t}\int\frac{\mathbf{u}^2}{2}dV = \int\nabla\cdot(*)dV - \int 2\sqrt{\frac{\mathrm{Pr}}{\mathrm{Ra}}}S_{ij}S_{ij}dV - \int\mathrm{Ha}^2\sqrt{\frac{\mathrm{Pr}}{\mathrm{Ra}}}\mathbf{j}^2dV + \int u_z\theta dV. \quad (8)$$

The volume integral of the divergence terms will vanish, hence the viscous dissipation and Joule dissipation are given by:

$$\varepsilon = 2\sqrt{\frac{\mathrm{Pr}}{\mathrm{Ra}}}S_{ij}S_{ij}, \quad \varepsilon_j = \mathrm{Ha}^2\sqrt{\frac{\mathrm{Pr}}{\mathrm{Ra}}}\mathbf{j}^2.$$

In magnetoconvection systems, temperature dissipation should also be included, which is defined as [24]:

$$\varepsilon_T(x,t) = \frac{1}{\sqrt{\mathrm{RaPr}}}(\nabla\theta)^2.$$

Under strong magnetic fields, dissipation is primarily dominated by Joule dissipation, yet the force balance is still predominantly characterized by the balance between buoyancy and pressure gradient, with viscous forces and Lorentz forces in secondary balance as shown in Fig. 14, which demonstrates that dissipation and forces increase gradually with Ra, but the main balance state remains unchanged. Both the dissipation and forces in Fig. 14 are spatially and temporally averaged, and although the forces in Fig. 14(b) are originally vectors, since their directions change little with time in the wall-mode flow state, the magnitudes of these forces are presented. The balance between pressure gradient and buoyancy dominates in the wall-mode interval. The difference between these two forces is balanced by the other three forces, among which inertial forces are two orders of magnitude smaller compared to the main balance interval. This is consistent with the RRBC study by Guzmán *et al.* [25], where in the cell flow state, inertial forces are always the smallest among all forces and exhibit a rapid decline with decreasing Ra number. As the flow state approaches the wall mode, buoyancy gradually replaces the Coriolis force as the dominant force in the balance. The wall-mode flow state is a quasisteady state. In DNS, there is no significant change in the flow state at different time steps. Global parameters such as Nu (Nusselt number) and Re (Reynolds number) also exhibit strong stability with respect to time. This is reflected in the momentum equation as

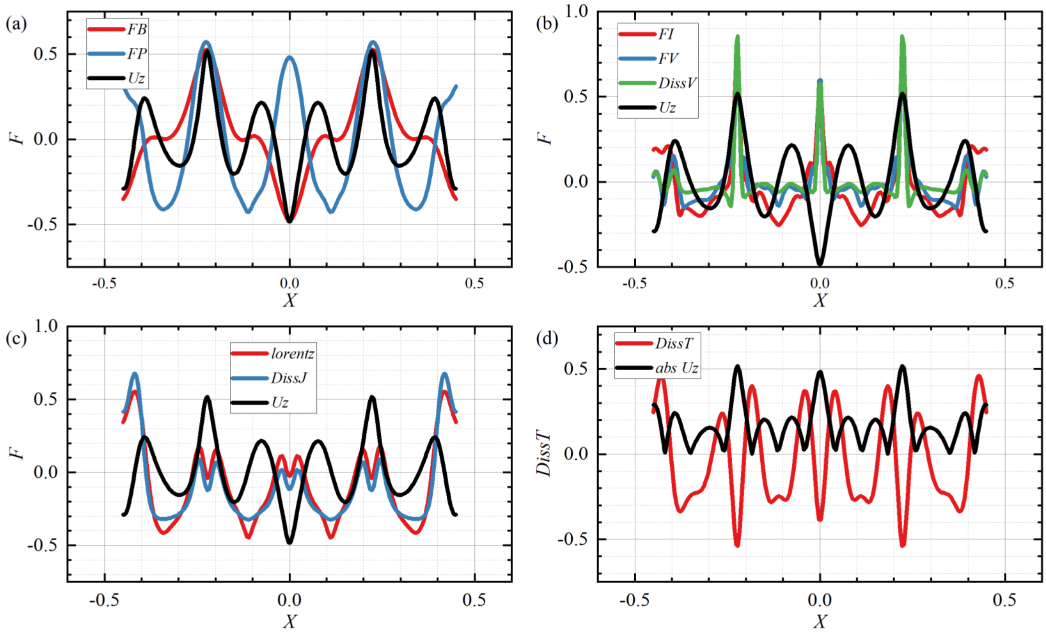


FIG. 15. (a) Distribution of buoyancy and pressure. (b) Distribution of viscous dissipation, inertial forces, and viscous forces. (c) Distribution of Lorentz forces and Joule dissipation. (d) Distribution of temperature dissipation (plot at $Z = 0$, $Y = -0.5 + 3.47\delta_{sh}$, $Ha = 200$, $\Gamma = 4$, and $Ra = 4.45 \times 10^5$).

$\partial \mathbf{u}/\partial t = 0$. Therefore, the wall mode can be considered to be in quasihydrostatic equilibrium, and it is understandable that the pressure gradient and buoyancy dominate the balance.

To investigate the dissipation and force distribution of the wall mode and its reverse flows on both sides, this study examines the position at $3.47\delta_{sh}$ as discovered by Liu *et al.* [7]. Figure 15(a) shows the distribution of buoyancy and pressure, with the distribution of $U_z$ superimposed on the figure. The peaks in the $U_z$ represent ascending flows, the valleys represent descending flows, and the maxima and minima at intermediate heights correspond to the reverse flows. Buoyancy is maximized at the positions of ascending flows and minimized at the positions of descending flows, indicating that the ascending and descending flows are primarily driven by buoyancy, while the pressure gradient is largest in the main flow region and smallest in the reverse flow region. The buoyancy exhibits a small plateau at the position of the reverse flow, suggesting that the generation of reverse flow is influenced by buoyancy.

The distribution of viscous dissipation is illustrated in Fig. 15(b), which is positively correlated with the magnitude of velocity. In the main flow region where velocities are high, viscous dissipation is significantly stronger. In contrast, the reverse flow regions, characterized by lower velocities, exhibit naturally weaker viscous dissipation. Figure 15(b) also displays the distributions of inertial forces and viscous forces; both forces are closely related to the flow velocity, peaking in the main flow region and forming a plateau in the reverse flow regions. At the junction positions of the two reverse flow wall modes, both viscous forces and inertial forces are at their minimum. The magnitudes of viscous dissipation, viscous forces, and inertial forces are all closely related to velocity, and although the reverse flows have lower velocities, they are still influenced by these forces.

Drawing on Busse's asymptotic theory, as presented in the work by Busse [6], on the straight line defined by the coordinates $X = 3.47\delta_{sh}$ and $Z = 0$, the velocity component in the $z$ direction can be approximated by the equation $w(3.47\delta_{sh}, y, 0) \approx 3\pi^4\sqrt{6\pi} \cdot (\mathrm{Ch})^{3/4} \cdot \exp(-\sqrt{3}\pi \cdot 3.47\delta_{sh}) \cdot \cos(\sqrt{2}\pi y)$. A meticulous examination of this velocity-distribution formula reveals a distinct

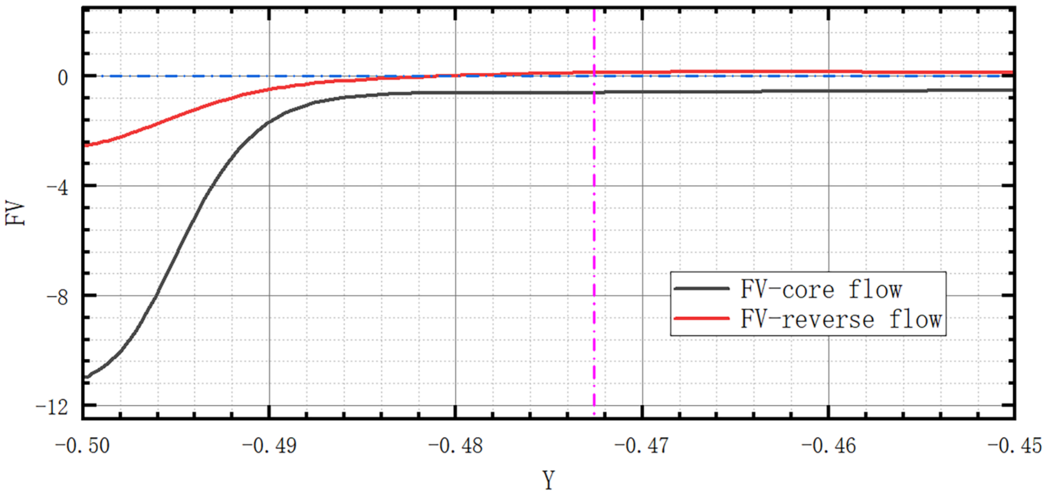


FIG. 16. Viscous force in the $z$ direction near the side wall (red line: plotted at $Z = 0$, $X = 0.0767$; black line: plotted at $Z = 0$, $X = 0$; blue dashed line: FV = 0; pink dashed line: $\mathrm{Y} = -0.5 + 3.47\delta_{sh}$, Ha = 200, $\Gamma = 4$, and Ra = $4.45 \times 10^5$).

cosine-shaped pattern. Notably, within the framework of this theoretical model, no reverse flow is predicted on either side of the core flow within the wall-mode regime. The fundamental premise underlying Busse's asymptotic theory assumes that the upper and lower plates adhere to free-slip boundary conditions. However, in practical scenarios, the presence of a no-slip boundary condition may introduce deviations from the theoretical predictions. This no-slip boundary condition could potentially be the root cause of the observed reverse flow. To further investigate this hypothesis, Fig. 16 showcases the distribution of the viscous force in the $z$ direction in the proximity of the side wall. The no-slip nature of the side wall leads to a significant augmentation of the viscous force. This enhanced viscous force effectively disrupts the restrictive influence that the vertical magnetic field typically exerts on the flow. In the regions of reverse flow, the direction of the viscous force is observed to be reversed. Moreover, the reverse flow is found to occur outside the Shercliff layer. In the bulk region, which is far removed from the Shercliff layer, the viscous force remains negligible until the horizontal wavelength diminishes to a certain extent. These findings provide crucial insights into the sequence of mode appearance. Given the aforementioned mechanisms, it can be deduced that the wall mode will emerge prior to the global mode. This sequence is a consequence of the complex interplay between the boundary conditions, viscous forces, and the influence of the magnetic field on the fluid flow. Understanding these relationships is essential for a comprehensive comprehension of the hydrodynamic behavior in such systems.

The distributions of Lorentz forces and Joule dissipation are shown in Fig. 15(c). Similar to the distribution of pressure gradients, Lorentz forces increase in the main flow region and decrease in the reverse flow regions. However, unusually, at the core position of the wall mode, the Lorentz forces are exceptionally reduced. The distribution of Joule dissipation, similar to the Lorentz forces, also shows an exceptional decrease at the core position. This indicates the presence of a small current region at the core area of the wall mode.

The distribution of temperature dissipation is illustrated in Fig. 15(d), where the absolute value of velocity has been taken to more clearly reveal the relationship between temperature dissipation and velocity. There is a negative correlation between temperature dissipation and the absolute value of velocity. In the core region where convective heat transfer is strongest, the temperature dissipation is minimal. In the reverse flow region, temperature dissipation also forms a relatively low plateau. Similar to diffusive heat transfer, temperature dissipation is indicative of temperature gradients. In areas with strong convective heat transfer, the flow carries heat along with it, resulting in naturally lower temperature dissipation. Conversely, at the intersection of flows in opposite directions, temperature dissipation increases. In summary, the reverse flow on both sides of the wall mode is influenced by the combined effects of buoyancy, viscosity, and inertia, with viscous dissipation also showing a slight enhancement in these areas. We also observed a region of low current in the core of the wall mode, which can provide certain guidance for engineering applications.

## IV. CONCLUSION

In this study, we employed DNS to thoroughly investigate the effects of varying strengths of external vertical magnetic fields $B_0$ and the aspect ratio $\Gamma$ on the MHD-RBC system within a closed rectangular cell within the range of wall mode validated by Xu *et al.* [8]. This study particularly focuses on the enhancement of global heat transfer with increasing magnetic field strength (measured by the increase in Ha), and the suppression of global heat transfer with increasing aspect ratio. The core objective of this study is to elucidate the role of heat transfer intensity and the volume fraction of wall mode in enhancing heat transfer within the wall-mode region.

Our comprehensive study on heat transfer and flow dynamics within the wall-mode region reveals that under stronger magnetic fields, the wall-mode state exhibits stronger heat transfer intensity. This improvement is evident through heightened flow velocity, enhanced convective heat transfer, and increased circulation. The faster flow and diminished diffusive heat transfer corroborate the increased convective heat transfer. While a lower aspect ratio can elevate global Nu, it does not intensify heat transfer within the wall-mode region. Reducing the aspect ratio narrows the intermediate zone, which lacks convective heat transfer, thus increasing the proportion of the cell effective for heat transfer and promoting overall heat transfer enhancement.

Under strong magnetic fields, the wall-mode flow state manifests as a wall-circulation state, which is similar to the wall-mode state in RRBC. Although wall mode in RRBC are known to drift around the central axis, this study quantified the positional changes of wall modes in DNS and found that wall modes do not exhibit drift as observed by Akhmedagaev *et al.* [10] in experiment. We found that the wall-mode region accounts for more than 92% of the overall momentum in the $z$ direction and also plays a dominant role in convective heat transfer. However, from the perspective of circulation, although the bulk circulation has a relatively low velocity and barely participates in heat transfer, it constitutes more than half of the total circulation. McCormack *et al.* [11] also found that bulk circulation exists in the intermediate region.

Temperature boundary layers occur in the wall mode's impact region, specifically in the upper part of the ascending flow and the lower part of the descending flow. These layers are absent at the wall-mode junction and in the bulk. The thickness of the temperature boundary layer diminishes with increasing Ra, and a stronger magnetic field further reduces this thickness. However, the aspect ratio has no effect on the temperature boundary layer's thickness, as it does not alter flow intensity. Reverse flow regions form on either side of the wall mode due to buoyancy-induced forces, with high velocities over a small area leading to a slight increase in viscous dissipation, inertial, and viscous forces. Notably, we observed a low-current region at the core flow of the wall mode, which could inform engineering design considerations.

Through DNS under varying magnetic fields and aspect ratios, we have delved into the complex patterns of convective heat transfer under strong magnetic fields. We anticipate that the outcomes of this study will provide substantial evidence for the design of RBC with strong magnetic field in future engineering applications. Ultimately, a strong magnetic field can enhance the heat transfer intensity of the wall-mode region, and a smaller aspect ratio can increase the effective heat transfer volume of the wall mode, both of which can intensify heat transfer. This has immense potential value in advanced passive thermal management and thermal engineering applications.

## ACKNOWLEDGMENTS

The authors acknowledge the support from CAS under Grants No. YSBR-087, No. XDB0790103, NSFC under Grants No. U24A6007 and the National Key R&D Program of China (No. 2022YFA1204100).

The authors report no conflict of interest.

[1] P. A. Davidson, *An Introduction to Magnetohydrodynamics* (Cambridge University Press, Cambridge, 2001).

[2] C. A. Jones, Planetary magnetic fields and fluid dynamos, Annu. Rev. Fluid Mech. **43**, 583 (2011).

[3] J. Schumacher, The various facets of liquid metal convection, J. Fluid Mech. **946**, F1 (2022).

[4] Y. Nakagawa, An experiment on the inhibition of thermal convection by a magnetic field, Nature (London) **175**, 417 (1955).

[5] S. Chandrasekhar, *Hydrodynamic and Hydromagnetic Stability* (Clarendon Press, Oxford, 1961).

[6] F. H. Busse, Asymptotic theory of wall-attached convection in a horizontal fluid layer with a vertical magnetic field, Phys. Fluids **20**, 024102 (2008).

[7] W. Liu, K. Dmitry, and J. Schumacher, Wall modes in magnetoconvection at high Hartmann numbers, J. Fluid Mech. **849**, R2 (2018).

[8] Y. Xu, S. Horn, and J. M. Aurnou, Transition from wall modes to multimodality in liquid gallium magnetoconvection, Phys. Rev. Fluids **8**, 103503 (2023).

[9] T. Zürner, F. Schindler, T. Vogt, S. Eckert, and J. Schumacher, Flow regimes of Rayleigh–Bénard convection in a vertical magnetic field, J. Fluid Mech. **894**, A21 (2020).

[10] R. Akhmedagaev, O. Zikanov, D. Krasnov, and J. Schumacher, Turbulent Rayleigh–Bénard convection in a strong vertical magnetic field, J. Fluid Mech. **895**, R4 (2020).

[11] M. McCormack, A. Teimurazov, O. Shishkina, and M. Linkmann, Wall mode dynamics and transition to chaos in magnetoconvection with a vertical magnetic field, J. Fluid Mech. **975**, R2 (2023).

[12] B. C. Houchens, L. M. Witkowski, and J. S. Walker, Rayleigh–Bénard instability in a vertical cylinder with a vertical magnetic field, J. Fluid Mech. **469**, 189 (2002).

[13] S. Bhattacharya, T. Boeck, D. Krasnov, and J. Schumacher, Wall-attached convection under strong inclined magnetic fields, J. Fluid Mech. **979**, A53 (2024).

[14] L. Chen, A. Pothérat, M.-J. Ni, and R. Moreau, Direct numerical simulation of quasi-two-dimensional MHD turbulent shear flows, J. Fluid Mech. **915**, A130 (2021).

[15] A. Pont-Vílchez, F. Trias, A. Gorobets, and A. Oliva, Direct numerical simulation of backward-facing step flow at and expansion ratio 2., J. Fluid Mech. **863**, 341 (2019).

[16] X. Zhang, R. E. Ecke, and O. Shishkina, Boundary zonal flows in rapidly rotating turbulent thermal convection., J. Fluid Mech. **915**, A62 (2021).

[17] B. Favier and K. Edgar, Robust wall states in rapidly rotating Rayleigh–Bénard convection, J. Fluid Mech. **895**, R1 (2020).

[18] Z. L. Lim, K. L. Chong, G.-Y. Ding, and K.-Q. Xia, Quasistatic magnetoconvection: heat transport enhancement and boundary layer crossing., J. Fluid Mech. **870**, 519 (2019).

[19] L. Zhang, J. Dong, and K.-Q. Xia, Exploring the plume and shear effects in turbulent Rayleigh–Bénard convection with effective horizontal buoyancy under streamwise and spanwise geometrical confinements, J. Fluid Mech. **940**, A37 (2022).

[20] H.-T. Zhu, L. Chen, and M.-J. Ni, Effects of wall conductivities on magnetoconvection in a cube, Phys. Rev. Fluids **9**, 043701 (2024).

[21] A. Teimurazov, M. McCormack, M. Linkmann, and O. Shishkina, Unifying heat transport model for the transition between buoyancy-dominated and lorentz-force-dominated regimes in quasistatic magnetoconvection, J. Fluid Mech. **980**, R3 (2024).

[22] A. Pandey, Thermal boundary layer structure in low-Prandtl-number turbulent convection, J. Fluid Mech. **910**, A13 (2021).
[23] R. Du puits, C. Resagk, A. Tilgner, F. Busse, and A. H.Thess, Structure of thermal boundary layers in turbulent Rayleigh–Bénard convection., J. Fluid Mech. **572**, 231 (2007).
[24] Y. Zhang, Q. Zhou, and C. Sun, Statistics of kinetic and thermal energy dissipation rates in two-dimensional turbulent Rayleigh–Bénard convection, J. Fluid Mech. **814**, 165 (2017).
[25] A. Guzmán, M. Madonia, J. Cheng, R. Ostilla-Mónico, H. Clercx, and R. Kunnen, Force balance in rapidly rotating Rayleigh–Bénard convection, J. Fluid Mech. **928**, A16 (2021).

*Correction:* A grant number in the Acknowledgments contained an error and has been fixed.